Applied Catalysis B: Environmental 136–137 (2013) 325–333

Contents lists available at SciVerse ScienceDirect

Applied Catalysis B: Environmental

journal homepage: www.elsevier.com/locate/apcatb

Effect of silver nanoparticles on TiO_2-mediated photodegradation of Alizarin Red S

Michele L. de Souza, Paola Corio*

Departamento de Química Fundamental, Instituto de Química, Universidade de São Paulo–PO Box 26.077, 05513-970 São Paulo/SP, Brazil

ARTICLE INFO

Article history:
Received 26 September 2012
Received in revised form 30 January 2013
Accepted 1 February 2013
Available online 16 February 2013

Keywords:
AOPs
Catalytic photodegradation efficiency
Alizarin Red S
Plasmonic photodegradation

ABSTRACT

Titanium oxide (TiO_2) is widely employed in photocatalysis and in organic solar cells despite certain efficiency shortcomings regarding the high e^-/h^+ pair recombination rate and wide E_{gap}. Wet chemistry immobilization of plasmonic Ag NPs onto commercial TiO_2 (P25) through a bifunctional linker molecule (3-mercaptopropionic acid) was employed as a strategy to overcome such shortcomings. This paper proposes the main photodegradation excitation mechanisms according to the irradiation energy source. The photodegradation of the textile dye Alizarin Red S (ARS) catalyzed by bare P25 and a P25-Ag composite was studied applying UV/visible and visible radiation. Under UV/visible radiation, the P25-Ag composite showed a 40% improvement in the photodegradation rate constant in comparison to the bare P25, a phenomenon assigned to the charge separation due to the Schottky barrier. After 180 min under visible radiation the ARS degradation was 80%, i.e. low P25 photosensitization, while the P25-Ag composite showed a 7% increase in the percentage degradation of the unsaturated compounds, which was attributed to the plasmonic local field enhancement at the TiO_2 surface.

1. Introduction

Titanium dioxide (TiO_2) has been largely employed as a photocatalyst in advanced oxidative processes (AOPs) due to its favorable environmental and economic properties (low toxicity, relatively high photocatalytic efficiency and low cost). Recent studies have revealed that the pure forms of the most common polymorphs of TiO_2 (anatase and rutile) exhibit lower photocatalytic activity than their mixtures. A mixture of approximately 80% anatase and 20% rutile has presented the best photoactivity in comparison with other fractions [1–3]. In this context, commercial TiO_2 sold as Degussa P25 (P25) presents properties which fulfill the requirements of AOPs in terms of its morphology, polymorphous fraction and surface area, and thus P25 has become a standard material in this field [1].

Semiconductor materials employed in photoconversion systems present a moderately wide energy gap between the conduction band (CB) and the valence band (VB), this separation being known as the band-gap energy (E_{gap}). The absorption of irradiation energy of certain wavelengths by a semiconductor (semiconductor excitation process) promotes electron transfer from the VB to the CB, leaving vacancies in the VB called holes. The photogenerated electron/hole (e^-/h^+) pair promotes the reduction and oxidation of species adsorbed at the surface of the semiconductor and induces oxidative degradation of species in solution through radical reactions [4]. TiO_2 is widely employed in wastewater treatment and in dye sensitized solar cells, although TiO_2 has some shortcomings such as a wide E_{gap} (approximately 3.2 eV) and high number of e^-/h^+ pair recombination events [5–7].

Only a small fraction of the sunlight that reaches the troposphere is UV radiation (3–5%), while visible radiation corresponds to approximately 40% of solar light [4]. Thus, employing TiO_2 as a photocatalyst requires the use of artificial UV sources, which increases the process costs. In addition, recombination events decrease the photocatalysis and photoconversion quantum efficiencies. In this regard, some important strategies to improve the TiO_2 efficiency must be considered: (i) extending or intensifying the TiO_2 excitation under visible irradiation; (ii) decreasing the e^-/h^+ pair recombination events [8–10].

Hybrid materials are commonly employed to extend the excitation of semiconductors toward the visible range. The photosensitization mechanism occurs through the indirect excitation under low energy radiation of colored compounds adsorbed at the surface of the semiconductor, such as dyes (Methylene Blue, Acid Orange 7), organic compounds (fullerene), and metallic complexes (ruthenium trisbipyridyl complex), [7,11,12] and the injection of electrons into the semiconductor CB [4,7,11]. If the oxidation of the adsorbed compound occurs irreversibly after the electron injection into the semiconductor CB, the radical cations generated induce further oxidation reactions with species in solution triggering their degradation [4,7,12]. In dye-sensitized solar cells, the charge of the

* Corresponding author. Tel.: +55 11 3091 3853; fax: +55 11 3091 3890.
E-mail address: paola@iq.usp.br (P. Corio).

0926-3373/$ – see front matter © 2013 Elsevier B.V. All rights reserved.
http://dx.doi.org/10.1016/j.apcatb.2013.02.012

absorbed compound is restored by a reversible redox pair, regenerating the hybrid material.

A semiconductor-metal nanoparticle catalyst (composite) is employed in order to promote charge separation after the direct excitation of the semiconductor under UV irradiation [9,13,14] and consequently increase the oxidation events at the TiO_2 surface positively affecting the photoinduced reactions such as photocatalysis [15,16]. At the semiconductor/metal interface a significant redistribution of charge occurs due to the overlap of the wave functions from the two sides, depending on the metal work function and semiconductor electron affinity. The formation of a depletion zone causes the bending of semiconductor VB and CB which, in an n-type semiconductor, are shifted downward in relation to the Fermi level. The transfer of the photoexcited electrons from the CB to the metal is facilitated, but the opposite scenario is prevented, forming the so-called Schottky barrier [17].

Noble metal nanoparticles (Ag, Au and Cu NPs) have distinct optical and catalytic properties which are not usually observed in the bulk metal. One of these distinct properties, the interaction of the conduction electrons at the NPs with the electromagnetic field at specific wavelengths, causes coherent electron cloud oscillations increasing the energy density at the NP surface; this phenomenon has being known as localized surface plasmon resonance (LSPR) [18]. LSPR causes the extinction of light (scattering and absorption) in the visible range, and concentrates energy at the NP surface. Thus, noble metal NPs immobilized on the semiconductor surface can either concentrate the local field energy under visible excitation through the LSPR effect or withdraw electrons from the TiO_2 CB under UV excitation due to the Schottky barrier, thereby enhancing photocatalytic or energy conversion efficiencies [10,19,20].

Successful improvements in TiO_2 photoactivity have been made regarding processes such as redox reactions, [9] water splitting [21,22] and energy conversion [23] employing such composites. Smith and Zhao studied the effect of Ag loading in TiO_2 nanorods on the photocatalytic effect of Methylene Blue under UV radiation by the charge separation effect and found the optimal concentration of 0.25 wt.% Ag. However, a low concentration, such as 0.09 wt.% Ag, presented improvement in the photocatalysis under UV radiation [24] and 0.05 wt.% Au presented good results for photoinduced hydrogen gas evolution catalyzed by Au-TiO_2 composites [10].

The most common procedures employed to immobilize metal NPs on the TiO_2 surface involve chemical reduction and photoreduction at the semiconductor surface under UV radiation [8]. Wet chemistry immobilization of CdSe nanoparticles by a bifunctional linker has shown good stability in studies on organic solar cells [25] and this approach was employed in this study to immobilize plasmonic Ag NPs on the TiO_2 surface.

The aim of this study was to develop a stable plasmonic P25-Ag composite by means of the wet chemistry immobilization of Ag NPs on the P25 surface employing a bifunctional linker, and to evaluate the plasmonic effect on its photocatalytic efficiency along with the charge separation and the P25 photosensitization. The catalytic efficiency of the P25-Ag composite is discussed in comparison to bare P25 in relation to the photocatalytic degradation of the textile dye Alizarin Red S (ARS) under UV/visible and visible radiation. ARS was employed as a proof-of-principle molecule and its degradation through the P25 photosensitization under visible excitation was also considered.

2. Experimental methods

2.1. Materials

Silver nitrate (purity >99%), 3-mercaptopropionic acid (MPA), sodium borohydride and ARS were purchased from Sigma–Aldrich, and TiO_2 P25 Aeroxide® from Degussa-Evonik. All chemicals were used without further purification. A high pressure Hg lamp 125 W Phillips HPL-N without the glass bulb was employed as the UV/visible radiation source. Museum Glass® (True Vue™) was placed between the lamp and the reaction vessel as a UV cut-off filter.

A Shimadzu UV-3101 PC spectrophotometer was used to monitor the decay in the ARS absorbance bands (260 nm and 422 nm) and to characterize the photocatalysts through Diffuse Reflectance (DR) spectroscopy using integrating sphere. Raman analysis was performed on a Renishaw InVia Reflex, coupled to a Leica DM 2500 M microscope, with 632.8 nm laser He/Ne excitation and a CCD detector. Infrared spectra were obtained on an FTIR Bomem MB-100 coupled with ATR. The emission lines spectrum was acquired on a Jobin Yvon U1000 Raman spectrometer coupled to a PMT detector.

The pore volume, pore diameter and surface area of the catalysts were determined from Brunauer–Emmet–Teller (BET) adsorption isotherms obtained on a Quantachrome Instruments analyzer, model NOVA 1200e, at liquid N_2 temperature. The amount of Ag in the composite was investigated by inductively coupled plasma atomic emission spectroscopy (ICP-AES) and measurements were obtained with a Spectro Ciros CCD. Transmission electron microscopy (TEM) and energy dispersive X-ray spectroscopy (EDX) were performed on a Philips CM 200 microscope operating at 200 kV and high-resolution TEM (HRTEM) images and EDX spectroscopy were performed on a TECNAI F20 X-Twin operating at 200 kV in order to confirm the morphology, dimensions and composition of Ag NPs in the composites. The light intensity was measured on Instruterm MRUR-202, MRUR-203 and LD-200 instruments to detect UVA, UVC and visible radiation, respectively.

2.2. Synthesis of Ag nanoparticles (Ag NPs)

The procedure applied to obtain Ag NPs was that described by Creighton et al. [26]. The reaction was carried out by the reduction of 1.0×10^{-3} mol L^{-1} aqueous $AgNO_3$ with an excess of an ice-cold aqueous solution of 2.0×10^{-3} mol L^{-1} $NaBH_4$ (1:3 v/v). The solutions were rapidly mixed with vigorous shaking in a sonicator to aid monodispersity. The Ag nanoparticle final suspension was yellow and a single sharp visible extinction band near 400 nm was observed.

2.3. P25-Ag composite synthesis (immobilization of Ag NPs on P25)

In this procedure, 87.5 mL of deionized water, 12.5 mL of Ag NPs suspension and 200 μL of 0.1 mol L^{-1} MPA/acetonitrile solution were kept under stirring in the dark for 10 h to yield MPA-capped Ag nanoparticles. Deionized water (12.5 mL) containing 0.5 g P25 was then added to this MPA-capped Ag suspension and kept under stirring for 24 h at room temperature. The resulting suspension was filtered, rinsed abundantly with deionized water to remove unbounded NPs, and dried under vacuum overnight. Finally, the orange solid (P25-Ag composite) obtained was ground in an agate mortar. The catalyst was characterized by BET, ICP-AES, TEM, and Raman and DR spectroscopies.

2.4. ARS adsorption isotherms and photocatalytic degradation measurements

Analysis to obtain the adsorption isotherms for the adsorption of ARS by P25 and P25-Ag composite, and the ARS photocatalytic degradation data was performed in an open-air glass cell connected to a thermostatic bath at 20.0 ± 0.2 °C under vigorous stirring. Adsorption measurements were taken during 60 min of interaction with the catalysts in the dark. The ARS

photocatalytic degradation was carried out with an aqueous suspension of 6.2×10^{-5} mol L^{-1} ARS (20 mg L^{-1}) containing 0.5 g L^{-1} of the photocatalyst. Other photodegradation experiments, such as photolysis and Ag NP-mediated degradation, were performed under similar conditions as the catalyzed photodegradation.

Aliquots of 4 mL for the adsorption and photodegradation experiments were acquired as a function of time, centrifuged twice at 13,400 rpm for 15 min and the UV/vis spectrum of the supernatant was recorded. The ARS degradation was monitored through the decolorization of the dye solution related to the decrease in the maximum absorbance at 422 nm (chromophoric groups) and the dye decomposition was monitored via the maximum absorbance decrease at 260 nm (unsaturated bonds). Error bars were calculated from triplicate experiments. First- and second-order kinetic equations for the ARS photocatalytic degradation were fitted considering the maximum absorbance at 422 nm as a variable as a function of the irradiation time (not shown). FTIR measurements of the dried precipitated catalysts were obtained in order to identify structural changes in the ARS after the adsorption onto the catalyst surface.

2.5. Light source and UV filter

UV/visible photocatalysis was performed using a high-pressure Hg lamp 125 W (Phillips HPL-N) with no glass bulb or radiation filter (Fig. S1 (A)), which presents strong emission lines at 365, 366 and 391 nm in the UV range and emission lines at 404, 408, 436, 492, 496, 546, 577, 579 and 691 nm in the visible range. Visible photocatalysis was performed by filtering the UV emission lines using Museum Glass® as a UV cut-off filter (transmittance spectrum is also shown in Fig. S1 (A)) which removes the UV lines at 365, 366 and 391 nm without significant interference in the visible emitted lines (Fig. S1 (B)).

The non-filtered light source provides 0.67 mW/cm^2 of UVC radiation, 2.50 mW/cm^2 of UVA radiation and 23.0×10^3 lx of visible light, while the UV filtered light source employing Museum Glass® provides 10.0 μW/cm^2 of UVC, 14.5 μW/cm^2 of UVA and 22.0×10^3 lx of visible radiation, filtering out about 99% of the UV light without significant interference in the visible light intensity.

3. Results and discussion

3.1. Characterization of the photocatalysts

ICP-AES measurements indicated the presence of 0.060 ± 0.001 wt.% Ag in the P25-Ag composite. The obtainment of Ag nanoparticles was confirmed from EDX spectra (Fig. 1(B)) and they had a similar size to the average size of the semiconductor, as shown on the TEM image (Fig. 1(A)). The sample was also investigated by HRTEM and, in order to confirm the NPs composition, fast Fourier transform (FFT) were performed on the acquired HRTEM images as an additional Ag identification technique. The Ag particle indicated on Fig. 1(C) according with the FFT inset (JCPDS 4-0783) appears attached above to another particle with different composition. Small Ag NPs attached to TiO_2 particles were also evidenced by HRTEM images (Fig. 1(D) and (F)) and the EDX spectra of the imaged areas (Fig. 1(E) and (G)) confirmed the presence of metallic Ag NPs in the composite along with the TiO_2 matrix and the Cu sample holder.

The Raman peaks in Fig. 1(H) at 395, 515, 636 and 794 cm^{-1} are assigned to the anatase phase of TiO_2, and the peak observed at 445 cm^{-1} is assigned to the rutile phase of TiO_2, which also presents a weak Raman peak at 610 cm^{-1} overlapped with a stronger anatase Raman peak at 636 cm^{-1} [27]. The Raman peaks have similar relative intensities for the two materials (P25 and P25-Ag composite),

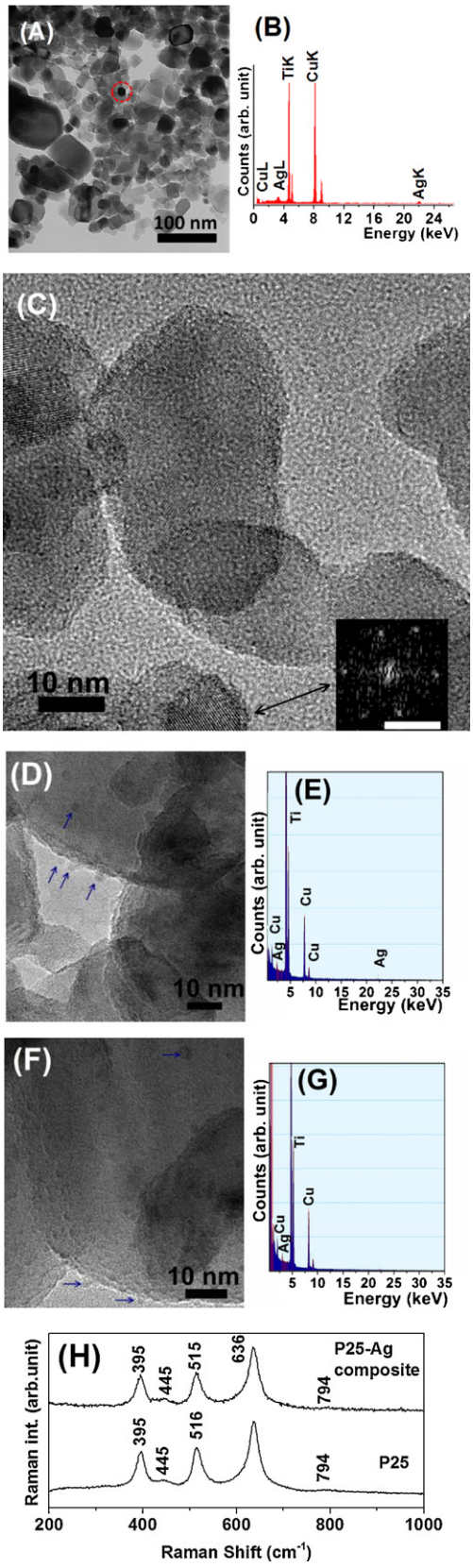

Fig. 1. (A) TEM image of P25-Ag composite; (B) EDX spectrum (Ag NP indicated in (A)); (C) HRTEM image of P25-Ag composite and (FFT pattern of the indicated Ag particle inset, scale bar 1 nm as reciprocal distance); (D) and (F) HRTEM images of P25-Ag composite of different regions (arrows indicate Ag particles); (E) and (G) EDX spectra of the respective imaged region; (H) Raman spectra of the photocatalysts under 632.8 nm laser excitation.

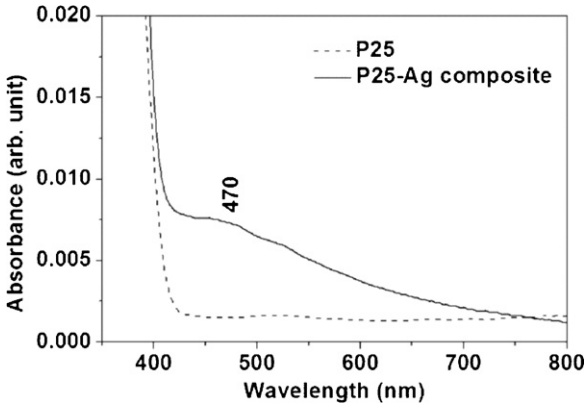

Fig. 2. DR spectra of P25 and the P25-Ag composite (Kubelka-Munk transformed).

and no significant peak shifts were observed, indicating no observable changes in the catalysts regarding the TiO_2 polymorphs before and after Ag NP immobilization. BET measurements (not shown) indicated that the P25 had a surface area of 45 $m^2\,g^{-1}$ and 1.7 nm pore diameter, while the P25-Ag composite had a surface area of 38 $m^2\,g^{-1}$ and 1.6 nm pore diameter. Considering the catalysts had similar surface area, composition and pore diameter, changes in their photochemical activities might be related to the presence of plasmonic Ag NPs.

The DR spectra for P25 and the P25-Ag composite, shown in Fig. 2, present strong absorption in the UV range assigned to the TiO_2 e^-/h^+ pair photoexcitation. The broad absorbance band with a maximum at ca. 470 nm observed only for the P25-Ag composite catalyst is assigned to the LSPR effect of the Ag NPs and confirms the presence of plasmonic structures in the semiconductor surroundings. Although colloidal Ag NPs in aqueous suspension presents strong LSPR excitation with maximum extinction at approximately 400 nm, the Ag NP surroundings in P25-Ag composite changed during the immobilization process, i.e. NP aggregates generated during the capping procedure and interaction with the P25 surface or even with MPA capping can cause modifications to the surrounding dielectrics of the NPs which results in a red-shift and broadening of the LSPR maximum peak.

3.2. Adsorption isotherms

The UV/vis spectrum for ARS (Fig. 3(A)) presents two main maxima bands (260 nm and 422 nm). The isotherm adsorption experiments were carried out monitoring the maximum absorption band at 422 nm. All experiments reached equilibrium after 30 min stirring in the dark at 20.0 ± 0.2 °C, as evidenced by the stabilization of the absorbance maxima on the UV/vis spectrum as a function of the adsorption time (not shown). The adsorption isotherm trends

Table 1
Langmuir isotherm model parameters of ARS adsorption by P25 and P25-Ag composite.

	$q_{max.}$ (μmol g^{-1})	$n_{max.}$ (μmol m^{-2})	K_{ads} (L μmol^{-1})
P25	119.7	2.64	0.137
P25-Ag composite	120.4	3.17	0.140

$q_{max.}$ = maximum number of molecules adsorbed per mass of adsorbate; $n_{max.}$ = maximum number of molecules adsorbed per adsorbate area; K_{ads} = adsorption constant.

are shown in Fig. 3(B) and the linearization graphs are shown in the inset.

The adsorption isotherm in Fig. 3(B) follows the behavior of the Langmuir model isotherm [28] for both catalysts (P25 and P25-Ag composite) at an ARS concentration of up to 56 mg L^{-1} (*Ceq* of 40 mg L^{-1}), with a *q* maximum of approximately 30 mg/g (mass of adsorbed dye/mass of catalyst). Herrmann and co-workers [29] proposed the Langmuir model isotherm for the adsorption of ARS on P25 at 30 °C for a concentration range of 5–30 mg L^{-1}, implying that ARS has a monolayer adsorption behavior on the P25 surface. These results corroborate the above-mentioned study even at higher initial concentrations, *Ci*. Similar ARS adsorption isotherm behavior was observed for the P25-Ag composite surface, as shown in Fig. 3(B). The linearization graphs (Fig. 3(B) inset) presented acceptable correlation coefficients and equivalent thermodynamic parameters for both catalysts, as shown in Table 1.

According to the results for the parameters shown in Table 1, it is possible to confirm that the addition of Ag NPs to the TiO_2 caused no thermodynamic changes in the behavior of ARS adsorption onto P25. These results also indicated that the concentration appropriate for studies on ARS photodegradation catalyzed by P25 and the P25-Ag composite, with the free ARS molecules in equilibrium with the adsorbed molecules at the photocatalyst surface, is around 22 mg L^{-1} (*Ceq* from 10 mg L^{-1}, Fig. 3(B)). In this study, heterogeneous photocatalysis experiments were carried out with an initial concentration of 6.2×10^{-5} mol L^{-1} (20 mg L^{-1}) ARS (aqueous solution) and 0.5 g L^{-1} of photocatalyst.

The surface interaction between ARS and the catalysts was probed by FTIR spectroscopy, as shown in Fig. 4.

At first glance, the FTIR spectra of the catalysts in Fig. 4 confirmed the similarity between P25 and the P25-Ag composite. The FTIR spectra for ARS-P25 and the ARS-P25-Ag composite in comparison to the bulk ARS spectrum (Fig. 4) show a decrease in the intensity of the following peaks: 1120 and 1232 cm^{-1} (assigned to the asymmetric stretching modes of the S=O moiety); 1196 cm^{-1} (assigned to C=O moiety); 1332 cm^{-1} (assigned to O—H stretching); splitting of the band at 1456 cm^{-1} (region where bands assigned to C—C stretching modes are located); and at 1668 cm^{-1} (assigned to C=O stretching at position 10 of ARS) [30–32].

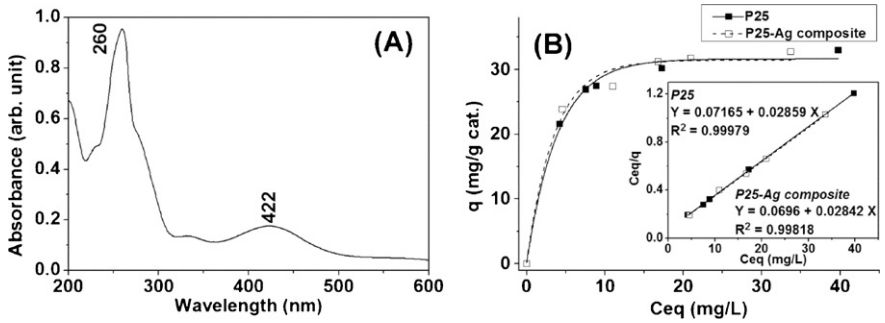

Fig. 3. (A) UV/vis spectrum of aqueous ARS; (B) adsorption isotherms at 20.0 ± 0.2 °C: ARS–P25 and ARS–P25-Ag composite (Langmuir model isotherm linearization graphs in inset).

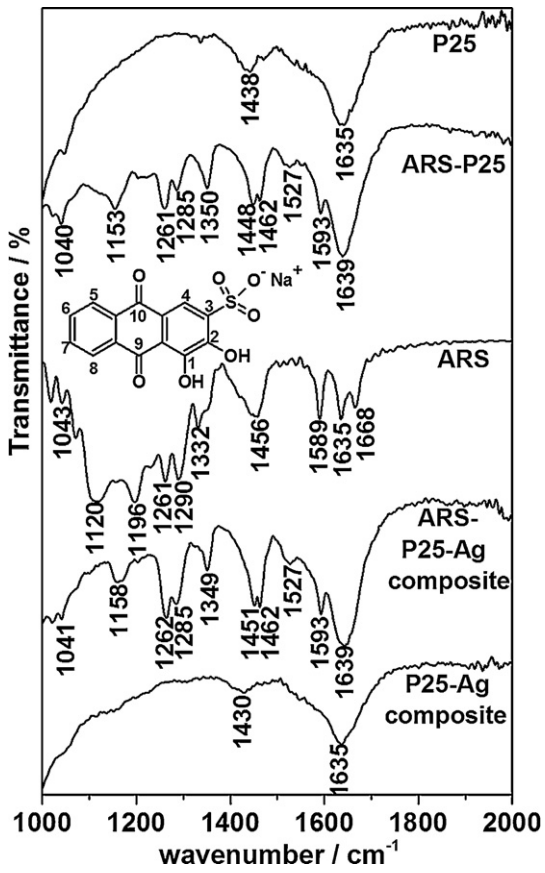

Fig. 4. FTIR spectra for P25, ARS-P25, bulk ARS (ARS molecular structure in inset), ARS-P25-Ag composite and P25-Ag composite.

After the ARS adsorption onto the P25 and P25-Ag composite surfaces, ARS peaks at 1261 and 1290 cm^{-1}, related to the C—O at positions 1 and 2, were intensified and the degree of splitting diminished. These peaks were more intense for the ARS-P25-Ag composite than for ARS-P25. Also, an enhancement in the peak at 1350 cm^{-1} occurs, related to C—O at position 1. The peaks which appear in the region around 1527 cm^{-1} may be related to a decrease in the ARS symmetry, consequently increasing the dipole moment of the molecule and enhancing the IR cross section.

According to the FTIR spectra for ARS-P25 and the ARS-P25-Ag composite in Fig. 4, and in agreement with the previous studies, [30–32] it was confirmed that, without changing the surface pH, ARS can interact with TiO_2 through chemisorption of the C—O at positions 1 and 2 or through 9C=O and 1C—O. The surface interaction causes the electronic redistribution of the dye structure, resulting in the bathochromic changes observed after ARS adsorption onto the semiconductor [30]. Furthermore, in agreement with the adsorption isotherm, which proposed similar adsorption behaviors and thermodynamic parameters for the two photocatalysts, the structures of the ARS adsorbed onto P25 and onto the P25-Ag composite analyzed by FTIR presented high similarity, suggesting that the P25 photosensitization may be roughly equivalent for the two systems and changes in the photocatalysis efficiency may be related to the Ag NP loading.

3.3. Catalyst efficiency: Photocatalytic rate constant

Solution decolorization, or relative intensity decay of the visible region absorbance band, was considered as indicative of ARS degradation through attack on the chromophore groups. Thus, ARS degradation was monitored through the maximum absorbance band at 422 nm in the UV/vis spectra as a function of the irradiation time. The absorption band at 260 nm was also monitored, although organic unsaturated photodegradation byproducts present strong absorption in this region and interfere with the direct observation of ARS photodegradation. Therefore, the 260 nm absorbance band was monitored to observe the degradation of unsaturated compounds, including ARS photodegradation byproducts.

Fig. 5(A) shows the UV/vis spectra of ARS photolysis (no catalyst added), and Fig. 5(B) shows the UV/vis spectra of the ARS photodegradation mediated by the P25-Ag composite. Both photocatalytic experiments under UV/visible radiation showed the appearance of no bands.

Under UV/visible excitation, ARS photodegradation occurred in the case of Ag NP-mediated and photolysis studies, however, Ag NPs caused greater degradation to the chromophoric groups than photolysis, and the generation of unsaturated byproducts hindered the observation of the 260 nm absorbance decay (Fig. 5(C) and (D)).

The catalytic degradation of ARS and colorless byproducts mediated by P25 and the P25-Ag composite occurred concomitantly. The ARS catalytic degradation mediated by the P25-Ag composite reached a maximum after approximately 30 min of irradiation while the degradation mediated by bare P25 reached a maximum after 45 min of irradiation (Fig. 5(D), absorbance band at 422 nm). Photodegradation of unsaturated compounds mediated by the P25-Ag composite (Fig. 5(C), 260 nm absorbance band) also occurred in a shorter time (45 min) than the catalysis mediated by bare P25 (60 min). Both results revealed that the presence of Ag NPs positively affects the photocatalysis kinetics under UV/visible radiation.

Fig. 6(A) shows UV/vis spectra of ARS photolysis under visible irradiation and no significant degradation was observed even after 180 min of irradiation. The UV/vis spectra of ARS photocatalyzed by the P25-Ag composite under visible excitation are shown in Fig. 6(B). The appearance of bands was not observed in any experiments.

Fig. 6(D) shows slight ARS degradation mediated by Ag NPs in comparison to photolysis under visible radiation. The generation of byproducts during photolysis and Ag NPs-mediated catalysis impairs the 260 nm absorbance decay observed in Fig. 6(C). As shown in Fig. 6(D), considerable ARS photocatalytic degradation mediated by bare P25 occurred, and the mechanism is assigned to the P25 photosensitization, as previously reported, [8,33] followed by the release of reactive compounds and degradation of unsaturated byproducts in the bulk solution (Fig. 6(C)).

Although the kinetics of the ARS photodegradation mediated by the P25-Ag composite was lower than that of the photodegradation mediated by bare P25, the P25-Ag composite catalysis presented continuous activity even after 90 min of irradiation (end of the bare P25-mediated catalysis, Fig. 6(C) and (D)). The composite catalysis presented higher ARS degradation than the bare P25 after 180 min. The greater efficiency of P25-Ag composite can be better observed by the photodegradation of unsaturated byproducts in Fig. 6(C), through the degradation after 90 min of irradiation being higher in comparison to bare P25 catalysis.

In our study, two figures of merit can be considered to assess the optimum photocatalyst: the photocatalysis rate constant and percentage of photodegradation. Although there was a distinct excitation mechanism in each case studied, a comparison between the catalysts considering the kinetics, an important feature of catalysis, applying a specific radiation source, can provide information related to improving the quantum efficiency. The photocatalysis apparent rate constant (k_{obs}) is proportional to the quantum yield of the photocatalysts. Thus, the catalyst efficiency can be evaluated through the normalization of the apparent rate constant of the P25-Ag composite to that of the catalyst considered as the standard, in this case bare P25 ($k_{ratio} = k_{obs\ P25\text{-}Ag}/k_{obs\ P25}$). All experiments fitted well a first-order reaction kinetics (not shown). The k_{obs} value

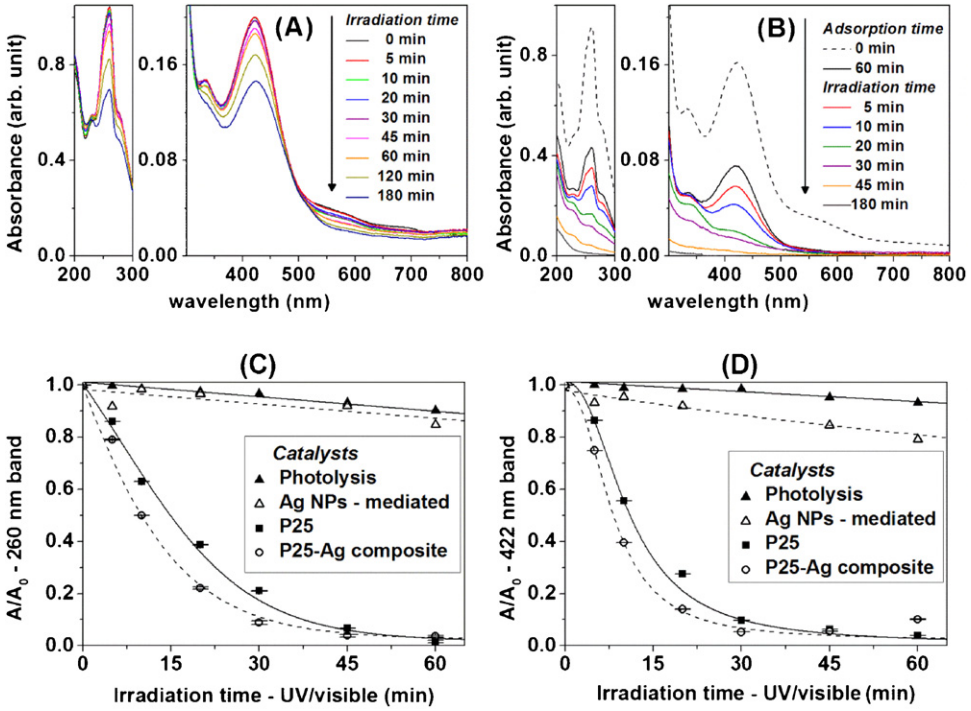

Fig. 5. UV/vis spectra of (A) photolysis and (B) photocatalysis mediated by P25-Ag composite as a function of UV/visible irradiation time (dashed line: ARS solution before addition of the catalyst). Relative absorbance decay monitored through absorbance bands in the UV/vis spectra as a function of the degradation time: (C) 260 nm and (D) 422 nm; catalytic degradation mediated by photolysis, Ag NPs, P25 and P25-Ag composite.

obtained for each catalyst, along with the k_{ratio} *s* values, are shown in Table 2.

Table 2 shows that, for the TiO_2 containing immobilized Ag NPs, the photocatalytic kinetics is positively affected under UV/visible radiation but negatively affected under visible radiation. The k_{ratio} values for the 260 nm and 422 nm absorbance bands in the degradation by UV/visible photocatalysis (1.37 and 1.19, respectively) indicated an improvement in the composite catalytic efficiency of approximately 40%. This behavior can be attributed mainly to the Schottky barrier formed between the Ag NPs and the P25, which

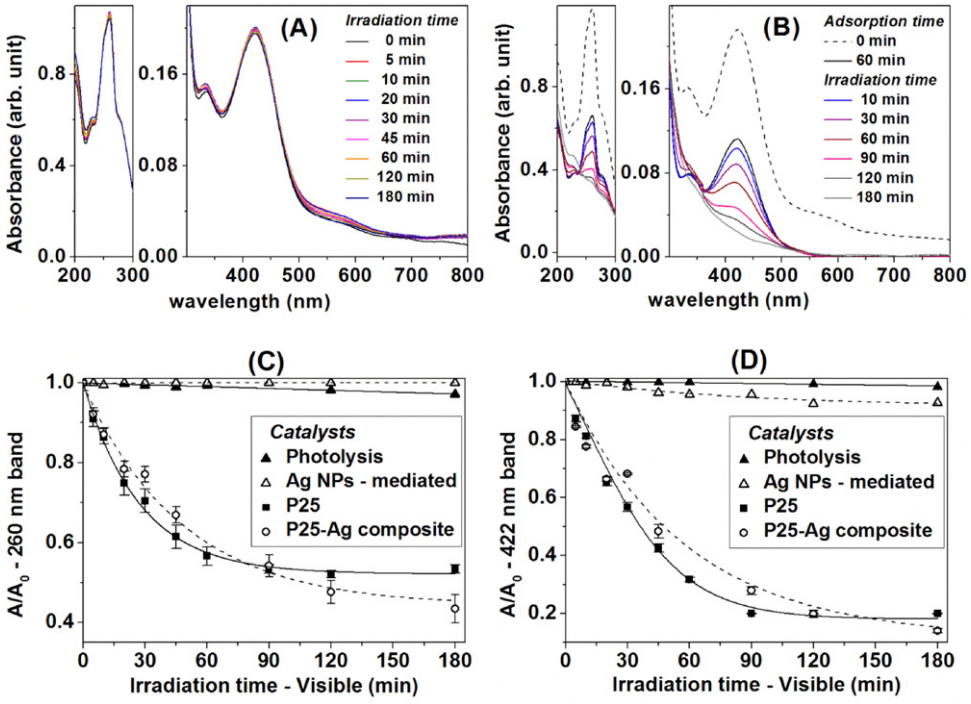

Fig. 6. UV/vis spectra for (A) photolysis and (B) photocatalysis mediated by P25-Ag composite as a function of visible irradiation time (dashed line: ARS solution before addition of the catalyst). Relative absorbance decay monitored via absorbance bands in the UV/vis spectra as a function of the degradation time: (C) 260 nm and (D) 422 nm; catalytic degradation mediated by photolysis, Ag NPs, P25 and P25-Ag composite.

Table 2
k_{obs} and k_{ratio} ($k_{obs\ P25\text{-}Ag}/k_{obs\ P25}$) to 260 nm and 422 nm absorbance bands under UV/visible and visible irradiation.

Absorbance bands	UV/visible irradiation			Visible irradiation		
	P25 k_{obs}	P25-Ag k_{obs}	k_{ratio}	P25 k_{obs}	P25-Ag k_{obs}	k_{obs}
	$\times 10^{-2}$ min^{-1}			$\times 10^{-2}$ min^{-1}		
260 nm	5.09	7.00	1.37	1.03	0.50	0.49
422 nm	7.54	9.00	1.19	1.69	0.79	0.46

causes electron scavenging and a decrease in the e^-/h^+ pair recombination events, as extensively reported in the literature [8,10,19].

On the other hand, although the maximum numbers of ARS molecules adsorbed to each catalyst were similar ($q_{max.}$ shown in Table 1), indicating that the P25 photosensitization should be equivalent in both cases of photocatalysis, a decrease in the photocatalysis apparent rate constant ratio was observed under visible radiation (k_{ratio} of 0.49 and 0.46 for absorbance bands at 260 nm and 422 nm, respectively), indicating that, at the beginning of the catalysis, the P25 photosensitization is strongly dominant, and the Ag NPs negatively affect the photosensitizing effect and thus the rate constant.

The photosensitization mechanism involves the conversion of the dye to a radical cation by the transfer of an electron from the excited dye to the semiconductor CB. The electron at the semiconductor CB causes reduction in the adsorbed molecular oxygen species to generate reactive oxidizing species such as $O_2^{\bullet -}$ and $^{\bullet}OH$ [4,30]. The radical cation and the reactive oxidizing species react with molecules in the bulk solution affecting the chromophoric groups of the dye and thus decolorizing the solution (422 nm absorbance decay) without a significant influence being observed on the unsaturated byproducts (slow absorbance band decay at 260 nm) [33]. Unsaturated byproducts, in turn, cannot sensitize P25 in the photocatalysis under visible light, and the bare P25 photodegradation reaches its end by the time that the colored compounds are mostly consumed, as observed in Fig. 6(C) and (D).

3.4. Catalyst efficiency: Photodegradation

The ARS degradation under visible radiation catalyzed by bare P25 presented an absorbance band plateau at 49% and 82% degradation ($A/A_0 = 0.51$ and 0.18 in Fig. 6(C) and (D)) with respect to the 260 nm and 422 nm absorbance bands, respectively. After most of the ARS had been degraded (82% of degradation), the P25 photosensitization was diminished, as discussed in Section 3.3. An incremental effect of plasmonic Ag NPs on the photocatalysis of the P25-Ag composite was observed as the photocatalysis proceeded, confirmed by the greater degradation of the unsaturated byproducts in comparison to bare P25 catalysis. An improvement of approximately 7% in the degradation was obtained for the P25-Ag composite in comparison to the bare P25 with respect to the 260 nm absorbance band after 180 min of irradiation, Fig. 6(C) and Table 3. Based on the experiments carried out, total mineralization did not occur even after 180 min of irradiation employing any of the catalysts, as observed by the remaining 260 nm absorbance band.

Decreases in the pH of 0.47 employing the bare P25 and 0.59 employing the P25-Ag composite were observed for the ARS photocatalytic degradation in comparison to the ARS initial solution pH. This result was attributed to the formation of organic acid byproducts, as reported in the literature [34].

3.5. Considerations regarding the enhanced photocatalysis

There are some propositions reported in the literature regarding the mechanism associated with the photocatalysis enhancement mediated by plasmonic composites under visible radiation, and the complexity of the present study offers the possibility for a comprehensive analysis of these available propositions according to the results discussed herein.

The thermal degradation at the plasmonic structure surface due to heat generation under irradiation at the plasmonic resonance is one of the propositions, which was experimentally confirmed not to be the case in the hot spot of the plasmon mode [35]. Indeed, in this study, a slight improvement in the ARS photodegradation for the 422 nm absorbance band mediated only by Ag NPs in comparison to photolysis was observed, but no degradation was observed for the 260 nm absorbance band under visible radiation after 180 min (Table 3). In the low thermal degradation observed in this study, the ARS chromophoric groups were the main target and there was only a weak influence on the photocatalysis of the unsaturated compounds (absorbance band at 260 nm), in agreement with Raman spectroscopic studies, which suggested that hydroxyanthraquinones adsorb to the surface of Ag colloids through the hydroxyl groups, which are the responsible for the color of this type of compound [36].

Regarding the improvement in the composite kinetics, two different possible scenarios have been discussed in the recent literature in relation to the plasmonic effect (Au and Ag NPs) for the semiconductor under visible radiation. One proposal considered the electron transfer from the plasmonic structure to the semiconductor CB, followed by the reduction of oxygen species adsorbed to the semiconductor surface and the simultaneous transfer of compensative electrons from a donor in solution to the plasmonic nanoparticle [8,10,19,21]. Another proposal addressed the radiative transfer of energy mediated by the optical local field enhancement at the semiconductor surface due to LSPR, boosting

Table 3
ARS degradation contents (decrease of the UV/vis absorbance bands) under UV/visible and visible irradiation after 180 min of irradiation.

	UV/visible irradiation		Visible irradiation	
	% decrease of the absorbance band at		% decrease of the absorbance band at	
	260 nm	422 nm	260 nm	422 nm
Photolysis	21.8	32.4	2.8	1.7
Ag NPs-mediated	36.3	35.0	0.0	7.5
P25	98.9	98.4	47.8	81.9
P25-Ag composite	97.8	97.5	54.6	85.9

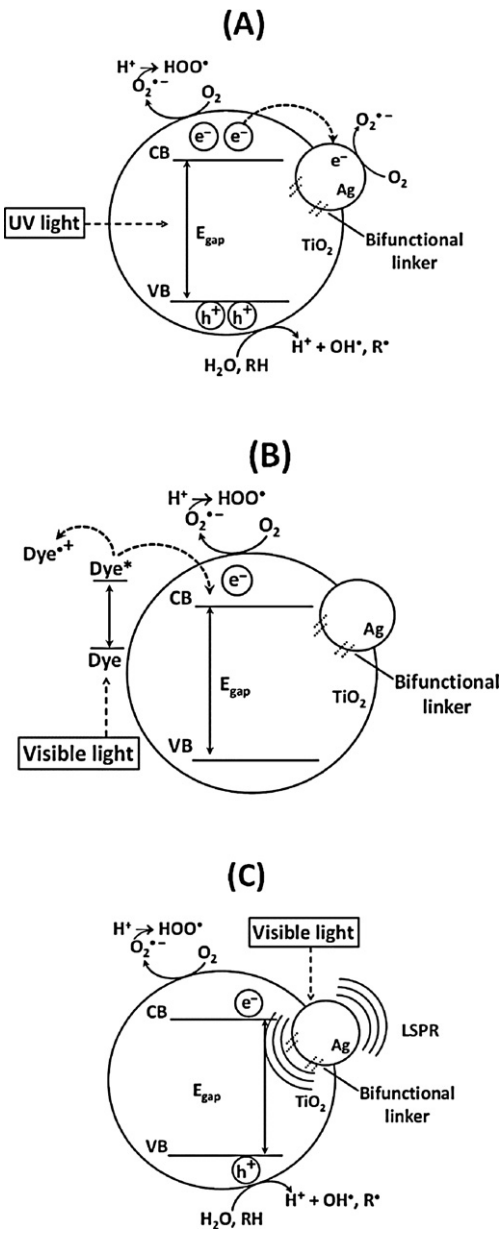

Scheme 1. Representation of excitation mechanisms associated with ARS photodegradation catalyzed by P25-Ag composite (bifunctional linker–MPA); (A) P25 direct excitation under UV irradiation; (B) P25 photosensitization under visible irradiation; (C) P25 indirect excitation by Ag NP LSPR under visible irradiation.

the excitation of e^-/h^+ pairs and thereby enhancing the photocatalytic efficiency [20,22,37].

Despite the small difference in energy between the Ag work function and TiO_2 electron affinity, charge transfer from the Ag NPs to the semiconductor CB remains feasible. In order to verify the electron injection from Ag NPs to TiO_2 CB on TiO_2/Ag composites, Linic and co-workers measured the evolution of the emission peak of charged TiO_2 at 680 nm and the red-shift of the plasmon peak in the electron deficient Ag NP in an environment without oxygen applying visible radiation. Their results indicated that there was no significant charge transfer from Ag to TiO_2, and the authors concluded that radiative transfer (local field intensification) more likely occurs [37].

Based on the above-mentioned considerations and the results obtained, Scheme 1 presents the excitation mechanisms discussed herein in relation to the ARS photodegradation catalyzed by P25-Ag composite as a function of the radiation energy (UV/visible or visible).

Scheme 1(A) shows the direct excitation of TiO_2 under UV/visible radiation, with energy greater than the TiO_2 E_{gap}, generating e^-/h^+ pairs. The holes (h^+) formed induce the oxidation of water molecules and organic compounds adsorbed onto the surface of the semiconductor, and the electrons (e^-) may follow two pathways: cause reduction reactions on the semiconductor surface or, as presented in this scheme, be withdrawn by the Ag NPs due to the Schottky barrier formed avoiding recombination events. Both pathways are followed in the electron transfer to molecules in solution. Hence the electron scavenging is beneficial to the charge carrier yield and, as observed experimentally, the catalyst efficiency increases.

In relation to the system under visible radiation, two photocatalytic mechanisms employing the P25-Ag composite must be taken in account: (i) the ARS-P25 photosensitization and (ii) the P25-Ag composite plasmonic effect. Scheme 1(B) shows the P25 photosensitization by the dye excitation followed by the transfer of an electron to the CB of the semiconductor releasing a radical cation to the solution, which induces the degradation of molecules in the bulk solution. The electron at the CB can induce the reduction of adsorbed oxygen molecules, generating reactive oxygen species, or can be withdrawn by the Ag NPs as indicated in Scheme 1(A) (under UV/visible radiation). However, the experimental results under visible radiation in the first minutes of photocatalysis, observed through the k_{ratio} (Table 2), indicated that the electron injection is not as beneficial to P25 photosensitization as it is to direct excitation of P25. Despite the fact that the photosensitization and the plasmonic structures acted simultaneously on the P25-Ag composite under visible radiation, their effects on the photocatalysis kinetics were not combined as would be expected, but instead the photosensitization effect overlapped with the LSPR effect at the beginning of the ARS photodegradation, and a decrease in the catalyst efficiency was observed compared to the bare P25.

Although the photocatalysis kinetics with P25-Ag composite was adversely affected, after the photosensitization decreased an increase in the ARS photodegradation content was detected. The local electromagnetic field enhancement due to Ag NP LSPR (Scheme 1(C)) results in the local excitation of the TiO_2 and the generation of e^-/h^+ pairs. This mechanism was observed experimentally after the almost complete degradation of ARS (80% degradation observed through the 422 nm absorbance band, Fig. 6(D)), i.e. through the degradation content of the unsaturated compounds (260 nm absorbance band, Fig. 6(C)) when the P25 photosensitization was not dominant. Therefore, the Ag NPs LSPR has an enhancement effect on ARS-P25-Ag composite photocatalysis.

4. Conclusions

A simple wet chemistry method for the immobilization of Ag NPs on the P25 surface leading to a catalytic composite material was performed. The catalytic efficiency of the P25-Ag composite under UV/visible and visible radiation was successfully observed through a comparison with the photodegradation of ARS employing bare P25. The new photocatalyst and the bare P25 showed several similar characteristics, including the composition, particle diameter and surface area. The isotherm for the adsorption of ARS on P25 and the P25-Ag composite behaved as a Langmuir model isotherm with similar thermodynamic parameters for the two catalysts and in the FTIR spectroscopy they showed equivalent ARS adsorption trends.

In the ARS photocatalytic degradation mediated by the P25-Ag composite, the rate constant under UV/visible excitation was improved compared to photocatalysis with the bare P25, attributed

to the formation of a Schottky barrier and charge separation. The P25-Ag composite efficiency under visible excitation was observed through the degradation, which continued even after the P25 photosensitization was significantly diminished (after almost complete removal of the ARS). The ARS degradation under visible radiation mediated by the P25-Ag composite after 180 min of irradiation, with respect to the absorbance band at 260 nm, showed an efficiency increase of 7% relative to the bare semiconductor catalyst. The results obtained in this study inferred that under visible radiation the P25 photosensitization is dominant for both catalysts at the beginning of the degradation, but the Ag NPs are disadvantageous to the photocatalysis kinetics, and after this effect is diminished it is possible to observe the local excitation of the photocatalyst through LSPR. This study, therefore, allowed a distinction to be made between the different photoexcitation mechanisms for the photocatalytic degradation of ARS and, more importantly, it was possible to differentiate the excitation mechanism according to the irradiation source and the degradation stage.

Acknowledgements

This work was supported by FAPESP (08/03636-5), CNPq and CAPES. The authors thank Central Analítica IQ-USP for support facilities, Prof. Pedro Kiohara (Physics Institute, USP) for the TEM measurements; Prof. Celly Mieko S. Izumi, Laboratório de Nanocaracterização UFSCar (FAPESP CEPID 98/14324-0 and INCTMN 08/57872-1 fellowships; CNPq INCTMN 573636/2008-7 fellowship) and Petrobras for the HRTEM measurements; Prof. Flavio Maron Vichi for the crystallographic database support; and the Contemporaneous Art Museum of USP (MAC-USP) for providing the Museum Glass®.

Appendix A. Supplementary data

Supplementary data associated with this article can be found, in the online version, at http://dx.doi.org/10.1016/j.apcatb.2013.02.012.

References

[1] T. Ohno, K. Sarukawa, K. Tokieda, M. Matsumura, Journal of Catalysis 203 (2001) 82–86.
[2] T. Ohno, K. Tokieda, S. Higashida, M. Matsumura, Applied Catalysis A 244 (2003) 383–391.
[3] L. Jing, S. Li, S. Song, L. Xue, H. Fu, Solar Energy Materials and Solar Cells 92 (2008) 1030–1036.
[4] J. Zhao, C. Chen, W. Ma, Topics in Catalysis 35 (2005) 269–278.
[5] R. Beranek, H. Kisch, Photochemical and Photobiological Sciences 7 (2008) 40–48.
[6] D.C. Hurun, K.A. Gray, T. Rajh, M.C. Thurnauer, Journal of Physical Chemistry B 109 (2005) 977–980.
[7] K. Rajeshwar, M.E. Osugi, W. Chanmanee, C.R. Chenthamarakshan, M.V.R. Zanoni, P. Kajitvichyanukul, R. Krishnan-Ayer, Journal of Photochemistry and Photobiology C 9 (2008) 171–192.
[8] S. Ko, C.R. Banerjee, J. Sankar, Composites: Part B 42 (2011) 579–583.
[9] T. Hirakawa, P.V. Kamat, Journal of the American Chemical Society 127 (2005) 3928–3934.
[10] E. Kowalska, O.O.P. Mahaney, R. Abe, B. Ohtani, Physical Chemistry Chemical Physics 12 (2010) 2344–2355.
[11] K. Vinodgopal, D.E. Wynkoop, P.V. Kamat, Environmental Science and Technology 30 (1996) 1660–1666.
[12] D. Chatterjee, S. Dasgupta, Journal of Photochemistry and Photobiology C 6 (2005) 186–205.
[13] A. Sclafani, J.-M. Herrmann, Journal of Photochemistry and Photobiology A 113 (1998) 181–188.
[14] T.A. Egerton, J.A. Mattinson, Journal of Photochemistry and Photobiology A 194 (2008) 283–289.
[15] L.G. Devi, K.M. Reddy, Applied Surface Science 257 (2011) 6821–6828.
[16] P. Sangpour, F. Hashemi, A.Z. Moshfegh, Journal of Physical Chemistry C 114 (2010) 13955–13961.
[17] K.W. Böer, Survey of Semiconductor Physics: Barriers, Junctions, Surfaces, and Devices, Vol. 2, Springer, New York, 1992.
[18] E. Hutter, J.H. Fendler, Advanced Materials 16 (2004) 1658–1706.
[19] Y. Tian, T. Tatsuma, Journal of the American Chemical Society 127 (2005) 7632–7637.
[20] K. Awazu, M. Fujimaki, C. Rockstuhl, J. Tominaga, H. Murakami, Y. Ohki, N. Yoshida, T. Watanabe, Journal of the American Chemical Society 130 (2008) 1676–1680.
[21] C.G. Silva, R. Juaréz, T. Marino, R. Molinari, H. Garcia, Journal of the American Chemical Society 133 (2011) 595–602.
[22] Z. Liu, W. Hou, P. Pavaskar, M. Aykol, S.B. Cronin, Nano Letters 11 (2011) 1111–1116.
[23] C.-S. Chou, R.-Y. Yang, C.-K. Yeh, Y.-J. Lin, Powder Technology 194 (2009) 95–105.
[24] W. Smith, S. Mao, G. Lu, A. Catlett, J. Chen, Y. Zhao, Chemical Physics Letters 485 (2010) 171–175.
[25] V. Subramanian, E.E. Wolf, P.V. Kamat, Journal of the American Chemical Society 126 (2004) 4943–4950.
[26] J.A. Creighton, C.G. Blatchford, M.G. Albretch, Journal of the Chemical Society, Faraday Transactions II 75 (1979) 790–798.
[27] R.J. Capwell, F. Spagnolo, M.A. DeSesa, Applied Spectroscopy 26 (5) (1972) 537–539.
[28] H.-J. Butt, K. Graf, M. Kappl, Physics and Chemistry of Interfaces, Second Edition, Wiley-VCH, Weinheim, Germany, 2006, pp. 189–191.
[29] H. Lachheb, E. Puzenat, A. Houas, M. Ksibi, E. Elaloui, C. Guillard, J-M. Herrmann, Applied Catalysis B 39 (2002) 75–90.
[30] Y.D. Iorio, E.S. Román, M.I. Litter, M.A. Grela, Journal of Physical Chemistry C 112 (2008) 16532–16538.
[31] P.M. Jayaweera, T.A.U. Jayarathne, Surface Science 600 (2006) L297–L300.
[32] M.L. de Souza, P. Corio, Vibrational Spectroscopy 54 (2010) 137–141.
[33] G. Liu, X. Li, J. Zhao, S. Horikoshi, H. Hidaka, Journal of Molecular Catalysis A: Chemical 153 (2000) 221–229.
[34] G. Liu, T. Wu, J. Zhao, H. Hidaka, N. Serpone, Environmental Science and Technology 33 (1999) 2081–2087.
[35] G. Baffou, C. Girard, R. Quidant, Physical Review Letters 104 (2010) 136805.
[36] M.V. Cañamares, J.V. Garcia-Ramos, C. Domingo, S. Sanchez-Cortes, Journal of Raman Spectroscopy 35 (2004) 921–927.
[37] P. Christopher, D.B. Ingram, S. Linic, Journal of Physical Chemistry C 114 (2010) 9173–9177.